AGU PUBLICATIONS

Geophysical Research Letters

RESEARCH LETTER
10.1002/2016GL071893

Key Points:
- Recent Arctic sea ice loss results in increased poleward eddy heat fluxes at 100 hPa over the central and eastern Eurasian regions
- Anomalous meridional wind and temperature fields coupled with climatological wave structure lead to the increased eddy heat fluxes
- These anomalies are dynamically linked through the propagation of stationary Rossby waves from the Barents-Kara sea ice reduction

Supporting Information:
- Supporting Information S1

Correspondence to:
J. Ukita,
jukita@env.sc.niigata-u.ac.jp

Citation:
Hoshi, K., J. Ukita, M. Honda, K. Iwamoto, T. Nakamura, K. Yamazaki, K. Dethloff, R. Jaiser, and D. Handorf (2017), Poleward eddy heat flux anomalies associated with recent Arctic sea ice loss, *Geophys. Res. Lett.*, *44*, 446–454, doi:10.1002/2016GL071893.

Received 29 MAR 2016
Accepted 13 DEC 2016
Accepted article online 14 DEC 2016
Published online 14 JAN 2017

Poleward eddy heat flux anomalies associated with recent Arctic sea ice loss

Kazuhira Hoshi[1], Jinro Ukita[2], Meiji Honda[1], Katsushi Iwamoto[3], Tetsu Nakamura[4], Koji Yamazaki[4], Klaus Dethloff[5], Ralf Jaiser[5], and Dörthe Handorf[5]

[1]Graduate School of Science and Technology, Niigata University, Niigata, Japan, [2]Faculty of Science, Niigata University, Niigata, Japan, [3]Mombetsu Municipal Office, Mombetsu, Japan, [4]Hokkaido University, Sapporo, Japan, [5]Alfred Wegener Institute, Potsdam, Germany

Abstract Details of the characteristics of upward planetary wave propagation associated with Arctic sea ice loss under present climate conditions are examined using reanalysis data and simulation results. Recent Arctic sea ice loss results in increased stratospheric poleward eddy heat fluxes in the eastern and central Eurasia regions and enhanced upward propagation of planetary-scale waves in the stratosphere. A linear decomposition scheme reveals that this modulation of the planetary waves arises from coupling of the climatological planetary wavefield with temperature anomalies for the eastern Eurasia region and with meridional wind anomalies for the central Eurasia region. Propagation of stationary Rossby wave packets results in a dynamic link between these temperature and meridional wind anomalies with sea ice loss over the Barents-Kara Sea. The results provide strong evidence that recent Arctic sea ice loss significantly modulates atmospheric circulation in winter to modify poleward eddy heat fluxes so as to drive stratosphere-troposphere coupling processes.

1. Introduction

Strongly motivated by the potential for improved predictability, possible relationships between rapid Arctic changes and extreme weather events in midlatitudes have been actively studied [*Kidston et al.*, 2015; *Kug et al.*, 2015]. Earlier work focused on regional aspects of the Arctic-midlatitude climate linkages such as the relationship between summer-to-fall sea ice anomalies in the Barents-Kara Sea and surface winter temperature anomalies in Siberia and eastern Asia [*Honda et al.*, 2009; *Orsolini et al.*, 2012]. Other studies have addressed the relationships between Arctic sea ice reduction with the meandering jet and changes in blocking frequencies [*Francis and Vavrus*, 2012], as well as with the negative phases of the Arctic Oscillation (AO) [*Thompson and Wallace*, 1998] and/or the North Atlantic Oscillation and consequent weather impacts in the Euro-Atlantic region [*Overland and Wang*, 2010; *Hopsch et al.*, 2012; *Jaiser et al.*, 2012], although debate continues [*Barnes*, 2013; *Screen et al.*, 2013; *Barnes and Screen*, 2015].

Lately, more attention has been given to stratosphere-troposphere coupling that potentially may link Arctic climate change to midlatitude climate [*Sun et al.*, 2015; *Nakamura et al.*, 2016; *Wu and Smith*, 2016]. The key question is whether Arctic sea ice and/or snow anomalies sufficiently modulate atmospheric circulation aloft so as to enhance the upward propagation of planetary-scale waves, which is known to affect tropospheric circulation and surface weather [*Baldwin and Dunkerton*, 2001; *Polvani and Waugh*, 2004]. Observational evidence is emerging that the reduction in Arctic sea ice, especially late-fall sea ice anomalies in the Barents-Kara Sea, results in increased poleward eddy heat fluxes thus enhanced upward propagation of planetary-scale waves, weakening of the stratospheric polar vortex, and consequent surface impacts [*Jaiser et al.*, 2013; *García-Serrano et al.*, 2015; *King et al.*, 2015; *Yang et al.*, 2016]. Numerical studies based on atmospheric general circulation model (AGCM) also show evidence for an active role of the stratosphere in the Arctic-midlatitude climate linkage; e.g., for snow anomalies [*Fletcher et al.*, 2009; *Peings et al.*, 2012] and sea ice anomalies [*Kim et al.*, 2014; *Nakamura et al.*, 2015, herein N15; *Jaiser et al.*, 2016]. There remain, however, questions regarding the strength of signals relative to natural variability [*Mori et al.*, 2014]; nonlinear atmospheric circulation responses from sensitivity to forcing regions in projected climate conditions [*Sun et al.*, 2015]; and the combined influence of sea ice, snow cover, and sea surface temperature forcings [*Cohen et al.*, 2014]. Moreover, previous studies have not studied detailed relationships between increased poleward eddy heat fluxes and upward propagating wave structure.

The aim of this study, which focuses on present climate conditions spanning the past three decades, is to better understand the temporal and spatial characteristics of the process that drives stratosphere-troposphere coupling, namely, the poleward eddy heat flux associated with the reduction in Arctic sea ice. To this end, we employ the linear decomposition scheme of *Nishii et al*. [2009] for the poleward eddy heat fluxes and examine individual temperature and meridional velocity fields for both reanalysis data and the simulation results.

2. Data and Methodology

This study used the Hadley Centre Sea Ice and Sea Surface Temperature data set version 1, 1° resolution sea ice concentration (SIC) data set [*Rayner et al*., 2003] and the Japanese 55-year Reanalysis (JRA-55) at 1.25° horizontal resolution [*Kobayashi et al*., 2015] for the analysis period of 1979–2015. For JRA-55, we first computed daily averaged data using the 6-hourly data. Then, JRA-55 atmospheric variables were linearly regressed on normalized SIC time series which was averaged over the Barents-Kara Sea (15–90°E, 70–85°N; see section S1 in the supporting information for sea ice time series and an associated SIC anomaly pattern) after both reanalysis and SIC data were detrended. Having conducted an extensive lead-lag correlation analysis, we determined that the December SIC index should be adopted. This is consistent with findings from other observational studies pointing out that late-fall to early-winter SIC anomalies are critical to atmospheric responses to Arctic sea ice reduction [*García-Serrano et al*., 2015; *King et al*., 2015; N15]. The sign of the regression coefficients is reversed to focus on the atmospheric response to a reduced state of Arctic sea ice.

We used data from the model simulations presented in N15, in which Arctic sea ice loss sensitivity experiments were conducted using the AGCM for the Earth Simulator (AFES) [*Ohfuchi et al*., 2004]. The experiments consisted of a pair of model runs, each integrated over the same annual cycle repeatedly for 60 years using the same climatological forcings and boundary conditions except for Northern Hemisphere sea ice. One run (CNTL) used SIC averaged over the high-sea ice period of 1979–1983, and the other (NICE) used SIC averaged over the low-sea ice period of 2005–2009. Both runs used the same sea surface temperature (SST) values from the CNTL period. At grid points where SIC fell below its value in the CNTL run, SST was set to the freezing point. Anomalies were defined by subtracting CNTL from NICE and thus represent anomalous atmospheric conditions associated solely with the reduction in Arctic sea ice (see section S1 and N15 for further details of the experiments). In our companion paper [*Jaiser et al*., 2016], we show a high degree of consistency between the AFES simulation results and the European Centre for Medium-Range Weather Forecasts ERA-Interim reanalysis data [*Dee et al*., 2011] in terms of the general characteristics of the stratosphere-troposphere link. In this study, we specifically focus on the changes in poleward eddy heat flux by a more detailed approach applied to the JRA-55 reanalysis data.

The poleward eddy heat flux is defined as v^*T^*, where v and T are the meridional wind and air temperature, respectively, and the superscript * denotes the deviation from the zonal mean. Poleward eddy heat flux is a key indicator of the upward propagation of planetary-scale waves, as it is proportional to the vertical component of the Eliassen-Palm flux in the transformed Eulerian mean framework [*Andrews and McIntyre*, 1976]. We calculate daily poleward eddy heat flux for both reanalysis data and simulation results, after an 11 day running mean is applied to the temperature and meridional wind data. All daily anomalies in this study are computed using daily climatological values, which are the 60 year mean of the CNTL run in the AGCM simulations and the 36 year mean of the reanalysis data in the observation. *Nishii et al*. [2009] decomposed the observed poleward eddy heat flux into three terms. Following their scheme, we decompose poleward eddy heat flux anomalies simulated in the AGCM experiments as follows:

$$[v^*T^*]_{\mathrm{NICE-CNTL}} = [v_c{}^*T_a{}^*] + [v_a{}^*T_c{}^*] + [v_a{}^*T_a{}^*]_a,$$

where the subscripts c and a denote the climatological mean and anomaly, respectively, and the square brackets denote a 60 year temporal average. We define the climatology as the 60 year mean of the high-sea ice run (CNTL) and anomalies as differences between daily NICE data and CNTL climatology (NICE − CNTL). The first and second terms are referred to as the linear terms in temperature anomaly (LTa) and in meridional wind anomaly (LVa), respectively. They represent poleward eddy heat flux anomalies formed by interactions between the climatological planetary wavefield and anomalous temperature and meridional wind fields, respectively. The last term is referred to as the nonlinear term, which is from both

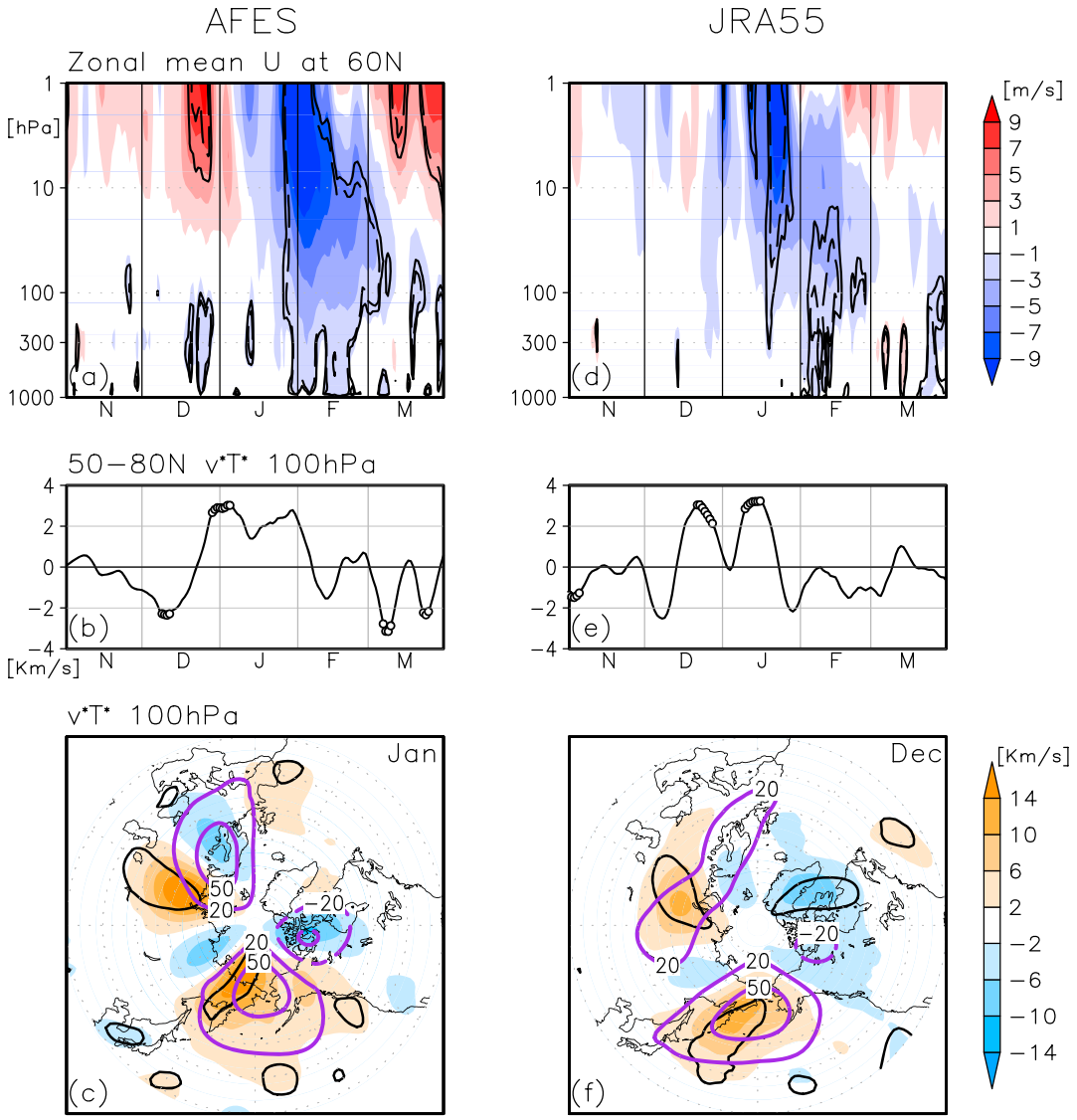

Figure 1. AGCM differences (NICE − CNTL) in (a) a time-height cross section of zonal-mean zonal wind at 60°N (shading; m s^{-1}), (b) a time series of 50–80°N mean poleward eddy heat flux at 100 hPa (K m s^{-1}), and (c) January-mean poleward eddy heat flux at 100 hPa (shading; K m s^{-1}). NICE reflects the light ice conditions of the 2005–2009 period, whereas CNTL is for the heavy ice conditions of 1979–1984. The purple contours in Figure 1c indicate the climatological (CNTL) poleward eddy heat flux. The JRA-55 anomalies of detrended (d) time-height cross section of zonal-mean zonal wind at 60°N (shading; m s^{-1}); (e) a time series of 50–80°N mean poleward eddy heat flux at 100 hPa (K m s^{-1}); and (f) December mean poleward eddy heat flux at 100 hPa (shading; K m s^{-1}) for 1979–2015, regressed on the normalized December mean Barents-Kara (15–90°E, 70–85°N) SIC index, are also shown. Note that the sign of the coefficients is reversed. The purple contours in Figure 1f indicate the climatological poleward eddy heat flux. The horizontal axes in Figures 1a, 1b, 1d, and 1e indicate the months. The solid (dashed) black lines in Figures 1a, 1c, 1d, and 1f indicate the statistical significance at the 90% (95%) level. The circles in Figures 1b and 1e indicate the statistical significance at the 95% level.

anomalous fields (see section S2 for details). To evaluate statistical significance we applied the two-sided Student's *t* test.

3. Results and Discussion

3.1. Wave-Mean Flow Interaction

Figures 1a and 1b show the time evolution of AGCM daily-mean anomalies of zonal-mean zonal wind at 60°N and poleward eddy heat flux averaged over 50–80°N at 100 hPa, respectively. Negative zonal wind anomalies

first appear in the upper stratosphere in early January, and significant signals subsequently propagate downward to the surface level in late January and February (Figure 1a). An increase in poleward eddy heat flux in late December and January precedes the weakening of the polar vortex (Figure 1b). Quantitatively, the increase in the poleward eddy heat flux averaged over January is about 19% of its climatological (CNTL) value. When we compare these results with the coefficients from the regression of JRA-55 on the December Barents-Kara Sea SIC index, there is striking resemblance in features such as the increased poleward eddy heat flux in December and January (Figure 1e) and the weakened stratospheric polar vortex and subsequent downward propagating signal (Figure 1d). *Kim et al*. [2014], N15, and *King et al*. [2015] each found similar results using slightly different methodologies on different data sets.

A question then arises as to whether there are any preferred locations for enhanced poleward eddy heat flux. There are indeed two centers of action in the poleward eddy heat flux climatology at the 100 hPa level (purple contours in Figures 1c and 1f). One is situated near the Barents-Kara Sea and the other over the Bering region, appearing consistently in both simulation and JRA-55 results. Note that we have used slightly different periods for the time averaging in each case (January for the simulations and December for JRA-55), which reflect the difference in their respective peak periods of poleward eddy heat flux (Figures 1b and 1e). It is straightforward to choose January for the simulations. In the reanalysis data, there are two peaks, December and January. We chose December as the analysis period because no statistically significant region appears in the January horizontal map (see section S3 for details).

The January-mean poleward eddy heat flux anomalies from the simulations (Figure 1c) and from the regression coefficients corresponding to 1 standard deviation of the December-mean Barents-Kara Sea SIC index (Figure 1f) are also shown. For both simulations and reanalysis data, positive poleward eddy heat flux anomalies appear in eastern Eurasia and its vicinity (herein the eastern Eurasia (EE) region). In addition, there is an area located approximately south of the Barents-Kara Sea (herein the central Eurasia (CE) region) with significant positive poleward eddy heat flux anomalies (Figures 1c and 1f). This is part of a dipole pattern with an area of negative flux anomalies situated to the west. Comparing the location of this dipole pattern with respect to the climatological center, we note that the reduction in Arctic sea ice leads to a shift and strengthening of the region of positive poleward eddy heat flux in CE.

3.2. Term-Wise Decomposition

Next, we analyze eddy heat fluxes in CE and EE by applying the decomposition scheme proposed by *Nishii et al*. [2009]. Figures 2a–2c show the maps of the linear and nonlinear terms that contribute to poleward eddy heat flux anomalies at 100 hPa in January, from the model simulations. For the EE region (50–80°N, 140°E–160°W; marked in Figure 2a), the dominant contributor is LTa, which accounts for most of the January peak in poleward eddy heat flux (Figure 2d). In fact, the LTa term makes up 59% of the January-mean poleward eddy heat flux over the EE region, while the LVa and nonlinear terms make up 22% and 19%, respectively. In contrast, Figure 2e shows the major contribution to the time series of eddy heat flux by the LVa term for the CE region (50–80°N, 50–90°E; marked in Figure 2b). The contributions from the LTa, LVa, and nonlinear terms are 8%, 58%, and 34%, respectively. Figure 2b also displays a dipole pattern with a positive anomaly over the CE region with a paired negative anomaly to the west, as discussed above. We analyzed the JRA-55 data in a similar manner and found that the positive anomalies in poleward eddy heat flux in EE for the peak period of December are dominated by the LTa term, whereas those in CE are dominated by the LVa term (see section S4). Interestingly, percentage-wise contributions of the LTa and LVa terms computed from JRA-55 are 60% and 61%, respectively, for EE and CE, again showing highly consistent results with the simulations.

3.3. Coupling Between Temperature and Wind Fields

Recognizing the importance of the LTa and LVa terms to the 100 hPa poleward eddy heat flux anomalies in the EE and CE regions, respectively, we take a step further to examine how the temperature and meridional wind fields are coupled to produce the resulting LTa and LVa patterns. We consider the simulation results first. Note that the climatological temperature field has a clear wave number 1 pattern (Figure 3b, shading) and that there is a dipole pattern in the climatological meridional wind field over the Eastern Hemisphere (i.e., a negative anomaly centered over Scandinavia and a positive anomaly over eastern Siberia in Figure 3 a, contours). Together, they constitute a climatological trough over Siberia at this level. The increase in the poleward eddy heat flux in the EE region is seen as resulting from coupling of the climatological southerly

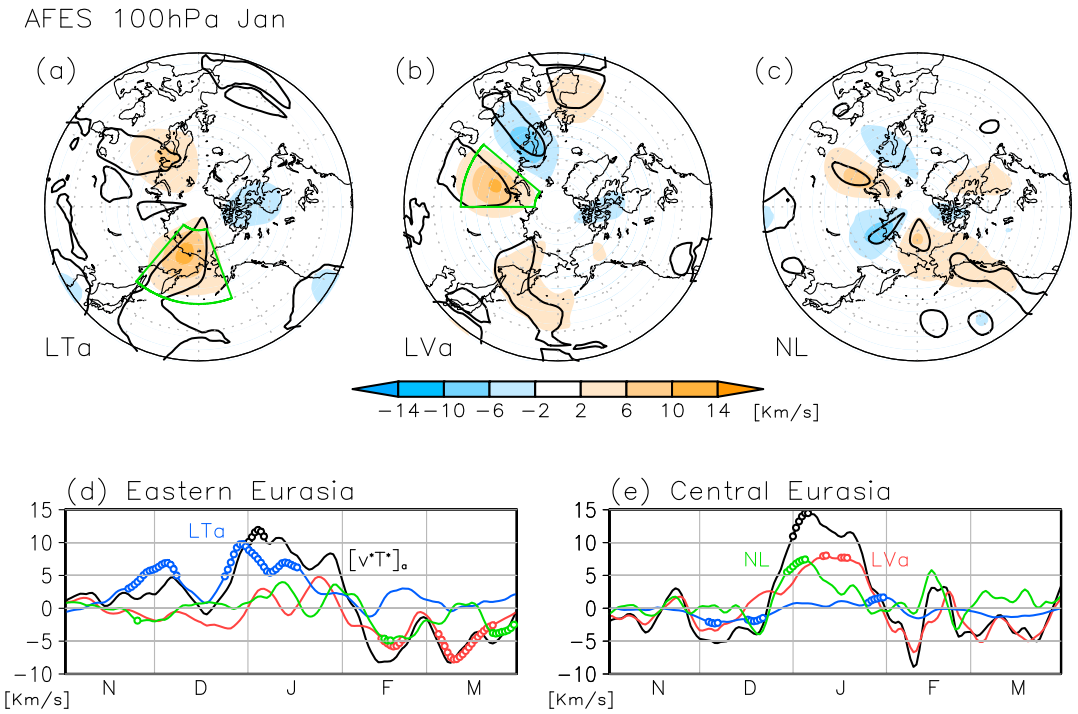

Figure 2. January-mean decomposed poleward eddy heat flux (K m s^{-1}) anomalies (a) [v_c*T_a*] (LTa), (b) [v_a*T_c*] (LVa), and (c) [v_a*T_a*] (NL) at 100 hPa, from the AGCM simulations. The green boxes in Figures 2a and 2b indicate the eastern Eurasia (50–80°N, 140°E–160°W) and central Eurasia (50–80°N, 50–90°E) regions, respectively. The black contours in Figures 2a–2c indicate the statistical significance at the 95% level. Time series of area-averaged poleward eddy heat flux anomalies and the decomposed components of the anomalies are shown for the (d) eastern Eurasia and (e) central Eurasia regions. The black lines indicate the poleward eddy heat flux anomalies, and the blue, red, and green lines indicate the LTa, LVa, and NL terms, respectively. The circles in Figures 2d and 2e indicate the statistical significance at the 95% level.

wind (contours in Figure 3a) with positive temperature anomalies (red shading in Figure 3a). In the CE region, eddy heat flux anomalies seen in Figure 1c are part of a wave train with three centers of action from the area west of the Iberian Peninsula. Similar tripole patterns are found both in LVa (Figure 2b, shading) and in meridional wind anomalies (Figure 3b, contours). These consistently present tripole patterns reveal that the increase in the poleward eddy heat flux in the CE region arises from coupling between negative meridional (northerly) wind anomalies and negative temperatures that are part of the climatological wave number 1 pattern (Figure 3b, shading).

Corresponding results from JRA-55 are generally in good agreement with those from the model simulations. For example, the wave number 1 pattern in the climatological temperature field is clearly visible (Figure 3d). The wave number 1 and 2 patterns in the climatological meridional wind field are highly consistent between the AGCM results and JRA-55, although the latter shows a stronger negative anomaly centered over Siberia (Figure 3c). In the EE region, a positive temperature anomaly coupled to climatological southerly wind induces an increase in the poleward eddy heat flux. In the CE region, similarly to the simulations, the dipole in meridional wind anomalies (positive over Scandinavia and negative over CE in Figure 3d) is superimposed on the negative temperature region that is part of the climatological wave number 1 temperature field. There are, however, differences between the JRA-55 data and model results, especially in the anomalous temperatures and meridional winds over northeastern Canada and the North Atlantic (Figure 3), which require further examination. Nonetheless, the spatial characteristics of the meridional wind and temperature fields over the CE and EE regions are remarkably consistent between JRA-55 and the model results.

3.4. Synthesis

The above analysis reveals in a systematic way how the coupling of temperature and meridional wind leads to increases in poleward eddy heat fluxes at the 100 hPa level in the CE and EE regions, as represented by the

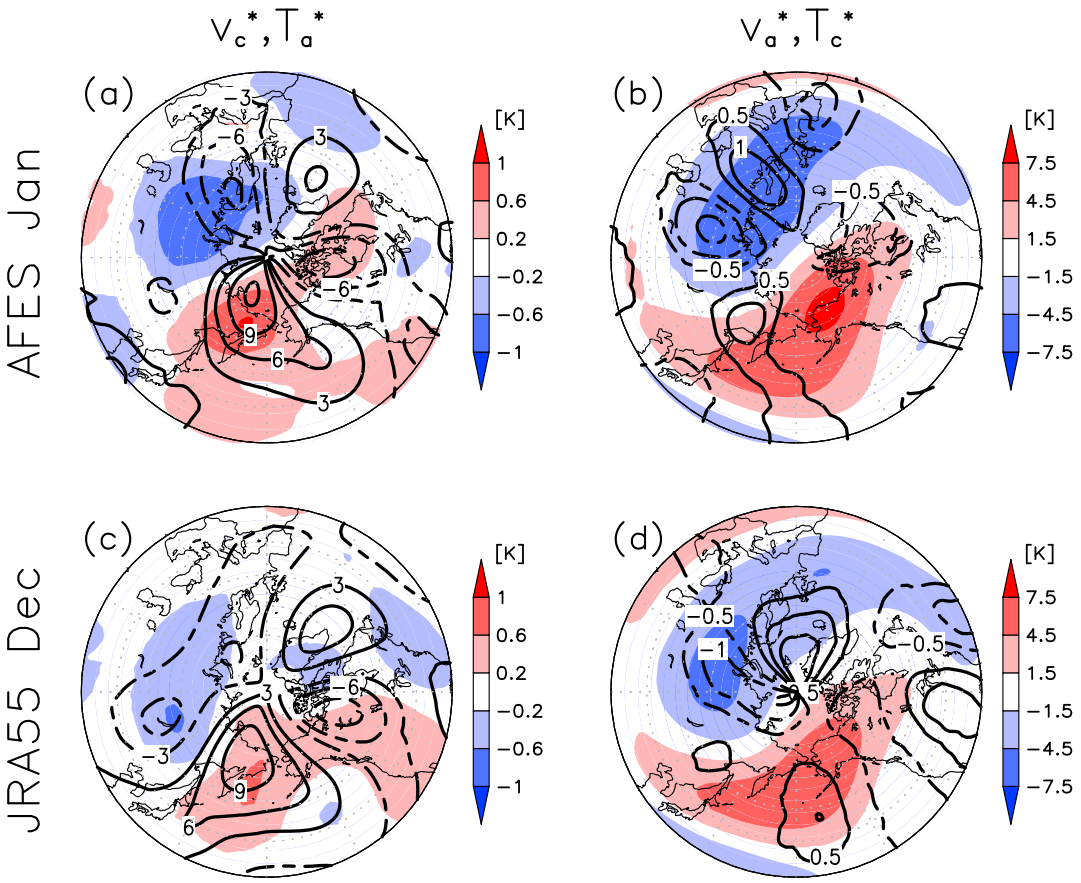

Figure 3. (a and c) Climatological meridional wind (v_c*; contours; m s^{-1}) and anomalous temperature (T_a*; shading; K) and (b and d) anomalous meridional wind (v_a*; contours; m s^{-1}) and climatological temperature (T_c*; shading; K), at 100 hPa from (Figures 3a and 3b) January-averaged AGCM results and (Figures 3c and 3d) December-averaged JRA-55 data.

linear terms. It is important to establish whether meridional wind and temperature anomalies in those two regions at the lower stratospheric level are dynamically linked with surface sea ice variability and to identify the processes responsible. Figure 4a captures the basic features of atmospheric teleconnection associated with Arctic sea ice reduction. Over the Barents-Kara Sea sector (approximately 30–90°E), positive anomalies of temperature (marked by A in Figure 4a) and positive anomalies of geopotential height (marked by B) appear in the troposphere as a result of the increased surface turbulent heating associated with sea ice loss (see also Figure 8 of N15 and Figures 3a and 4 of *Honda et al.* [2009] for a detailed discussion). Since the wave activity flux is parallel to the group velocity of stationary Rossby wave packets [*Takaya and Nakamura*, 2001], Figure 4a indicates upward propagation of Rossby waves from the Barents-Kara Sea sector into a region of positive height anomaly in the stratosphere (marked by E in Figure 4a). Along this path, a wave train appears to be composed of two positive geopotential height anomalies, one over the Barents-Kara Sea sector in the troposphere which extends to the lower stratosphere and the other over the longitudinal sector that includes the EE region in the stratosphere, with a negative geopotential height anomaly in between (marked by C).

The positive geopotential height anomalies marked by B is consistent with the dipole in the anomalous meridional wind field in the CE region at 100 hPa (Figure 3a). The stratospheric positive temperature anomaly, marked by D, with westward tilting structure and with a quarter wavelength shift with respect to the positive height anomaly (marked by E) is also consistent with the horizontal pattern of temperature anomalies in the EE region at 100 hPa (see Figure 3a). JRA-55 data show good agreement with the simulation results in terms of temporal and spatial characteristics of eddy hear flux anomalies, although the details are somewhat different, e.g., negative temperature anomalies in the upper stratosphere and negative geopotential height anomalies in the Western Hemisphere (Figure 4b). In the model experiments the vertical component of wave

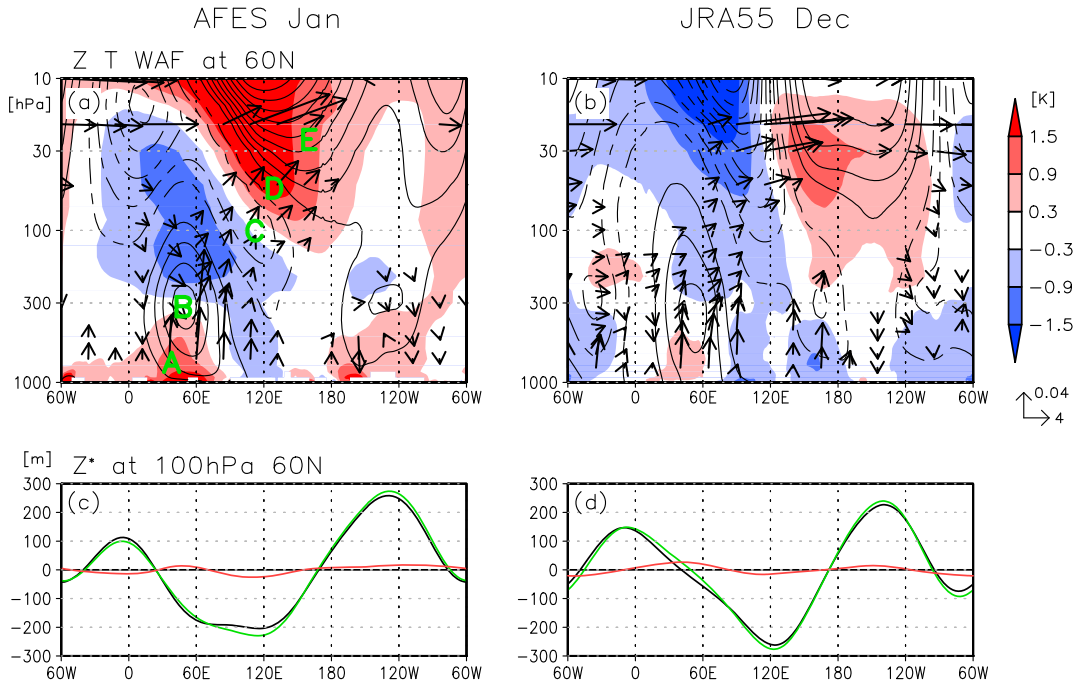

Figure 4. (a) January-mean longitude-height cross section at 60°N of AGCM differences (NICE − CNTL) in temperature (shading; K) and geopotential height (contours; m). The arrows indicate the zonal and vertical components of wave activity flux ($m^2 s^{-2}$), as defined by *Takaya and Nakamura* [2001]. (b) Same as in Figure 4a but from the JRA-55 data corresponding to 1 standard deviation of the December-averaged Barents-Kara SIC. For Figures 4a and 4b, the black lines are drawn for every 10 m and the dashed lines indicate the negative values. The 0 lines are omitted. The vectors are scaled by the reciprocal square root of the density, and the small vectors are not plotted. (c) Geopotential height anomalies (m) at 60°N from the respective zonal means of CNTL (black), NICE (green), and NICE − CNTL (red). (d) Climatology (black), regression coefficients (green) of geopotential height anomalies (m) at 60°N from their respective zonal means associated with 1 standard deviation of the December-averaged Barents-Kara SIC index, and their sum (red).

activity flux is nearly absent in the troposphere, except over the Barents-Kara region, even if we prescribe sea ice anomalies over the entire Northern Hemisphere (see section S5 for more details). The above results strongly suggest that stationary Rossby wave propagation from the Barents-Kara region is a major driver of the meridional wind and temperature anomalies and associated increases in the poleward eddy heat fluxes in the CE and EE regions at the lower stratospheric level.

In Figures 4c and 4d it is clear that deviations from the respective zonal mean averages of geopotential height anomalies at 100 hPa, both in the simulation results and observed atmospheric variability that is linearly related to the December Barents-Kara SIC, modulate the wave structure in the lower stratosphere in such a way that a climatological trough over Siberia is deepened through the processes described above. Thus, the results show constructive linear wave interference on the planetary wavefield [e.g., *Fletcher and Kushner*, 2011; *Smith and Kushner*, 2012], which arises from Arctic sea ice loss under present climate conditions (see the discussion in *Sun et al*. [2015] in the context of projected sea ice loss). It is notable that surface disturbance from a rather small region of the Barents-Kara Sea results in planetary-scale modulation of the stratospheric wave structure.

4. Conclusions

We have investigated how the spatial and temporal characteristics of poleward eddy heat flux, and therefore of the upward propagation of planetary waves, are modulated in response to the present-day reduction in Arctic sea ice. Both the AGCM simulations and the reanalysis data reveal that the increased poleward eddy heat fluxes at the lower stratospheric level in the CE and EE regions result from Arctic sea ice loss. These increases in the two regions are due to constructive coupling of the climatological planetary wave structure

with anomalous meridional wind and temperature fields, respectively, which are dynamically linked through the propagation of stationary Rossby waves emanating from the Barents-Kara Sea region.

Previous studies have examined and characterized anomalous poleward eddy heat fluxes in the northern high latitudes in conjunction with different stratospheric conditions, e.g., with AO and the vortex strength [*Polvani and Waugh*, 2004; *Garfinkel et al*., 2010] or with stratospheric sudden warming events [*Nishii et al*., 2009]. In comparison, this study provides a detailed three-dimensional picture of the way the recent Barents-Kara sea ice loss has modified the poleward eddy heat flux field in the lower stratosphere and subsequently affects the stratospheric wave structure, which likely plays a key role in the Arctic-midlatitude climate linkages under present climate conditions.

Acknowledgments

We thank K. Nishii and K. Takaya for their valuable discussions and comments. The JRA-55 data set was provided by the Japan Meteorological Agency (http://jra.kishou.go.jp/JRA-55/). The HadISST1 data were obtained from the Met Office Hadley Centre website (http://www.metoffice.gov.uk/hadobs/hadisst/). This study was supported by the Green Network of Excellence Arctic Climate Change Research Project and Arctic Challenge for Sustainability Project. We thank the AFES development team at the Japan Agency for Marine-Earth Science and Technology, at which the AFES simulations were performed using the Earth Simulator.

References

Andrews, D. G., and M. E. McIntyre (1976), Planetary waves in horizontal and vertical shear: The generalized Eliassen-Palm relation and the mean zonal acceleration, *J. Atmos. Sci.*, *33*, 2031–2048, doi:10.1175/1520-0469(1976)033<2031:PWIHAV>2.0.CO;2.

Baldwin, M. P., and T. J. Dunkerton (2001), Stratospheric harbingers of anomalous weather regimes, *Science*, *294*, 581–584, doi:10.1126/science.1063315.

Barnes, E. A. (2013), Revisiting the evidence linking Arctic amplification to extreme weather in midlatitudes, *Geophys. Res. Lett.*, *40*, 1–6, doi:10.1002/grl.50880.

Barnes, E. A., and J. A. Screen (2015), The impact of Arctic warming on the midlatitude jet-stream: Can it? Has it? Will it?, *WIREs Clim. Change*, *6*, 277–286, doi:10.1002/wcc.337.

Cohen, J., et al. (2014), Recent Arctic amplification and extreme mid-latitude weather, *Nat. Geosci.*, *7*, 627–637, doi:10.1038/ngeo2234.

Dee, D. P., et al. (2011), The ERA-interim reanalysis: Configuration and performance of the data assimilation system, *Q. J. R. Meteorol. Soc.*, *137*, 553–597, doi:10.1002/qj.828.

Fletcher, C. G., and P. J. Kushner (2011), The role of linear interference in the annular mode response to tropical SST forcing, *J. Clim.*, *24*, 778–794, doi:10.1175/2010JCLI3735.1.

Fletcher, C. G., S. C. Hardiman, P. J. Kushner, and J. Cohen (2009), The dynamical response to snow cover perturbations in a large ensemble of atmospheric GCM integrations, *J. Clim.*, *22*, 1208–1222, doi:10.1175/2008JCLI2505.1.

Francis, J. A., and S. J. Vavrus (2012), Evidence linking Arctic amplification to extreme weather in mid-latitudes, *Geophys. Res. Lett.*, *39*, L06801, doi:10.1029/2012GL051000.

García-Serrano, J., C. Frankignoul, G. Gastineau, and A. de la Cámara (2015), On the predictability of the winter Euro-Atlantic climate: Lagged influence of autumn Arctic sea ice, *J. Clim.*, *28*, 5195–5216, doi:10.1175/JCLI-D-14-00472.1.

Garfinkel, C. I., D. L. Hartmann, and F. Sassi (2010), Tropospheric precursors of anomalous Northern Hemisphere stratospheric polar vortices, *J. Clim.*, *23*, 3282–3299, doi:10.1175/2010JCLI3010.1.

Honda, M., J. Inoue, and S. Yamane (2009), Influence of low Arctic sea-ice minima on anomalously cold Eurasian winters, *Geophys. Res. Lett.*, *36*, L08707, doi:10.1029/2008GL037079.

Hopsch, S., J. Cohen, and K. Dethloff (2012), Analysis of a link between fall Arctic sea ice concentration and atmospheric patterns in the following winter, *Tellus, Ser. A*, *64*, 18624, doi:10.3402/tellusa.v64i0.18624.

Jaiser, R., K. Dethloff, D. Handorf, A. Rinke, and J. Cohen (2012), Impact of sea ice cover changes on the Northern Hemisphere atmospheric winter circulation, *Tellus, Ser. A*, *64*, 11595, doi:10.3402/tellusa.v64i0.11595.

Jaiser, R., K. Dethloff, and D. Handorf (2013), Stratospheric response to Arctic sea ice retreat and associated planetary wave propagation changes, *Tellus, Ser. A*, *65*, 19375, doi:10.3402/tellusa.v65i0.19375.

Jaiser, R., T. Nakamura, D. Handorf, K. Dethloff, J. Ukita, and K. Yamazaki (2016), Atmospheric autumn and winter response to Arctic sea ice changes in reanalysis data and model simulations, *J. Geophys. Res. Atmos.*, doi:10.1002/2015JD024679.

Kidston, J., A. A. Scaife, C. Hardiman, D. M. Mitchell, N. Butchart, M. P. Baldwin, and L. J. Gray (2015), Stratospheric influence on tropospheric jet streams, storm tracks and surface weather, *Nat. Geosci.*, *8*, 433–440, doi:10.1038/ngeo2424.

Kim, B.-M., S.-W. Son, S.-K. Min, J.-H. Jeong, S.-J. Kim, X. Zhang, T. Shim, and H.-J. Yoon (2014), Weakening of the stratospheric polar vortex by Arctic sea-ice loss, *Nat. Commun.*, doi:10.1038/ncomms5646.

King, P. M., M. Hell, and N. Keenlyside (2015), Investigation of the atmospheric mechanisms related to the autumn sea ice and winter circulation link in the Northern Hemisphere, *Clim. Dyn.*, doi:10.1007/s00382-015-2639-5.

Kobayashi, S., et al. (2015), The JRA-55 reanalysis: General specifications and basic characteristics, *J. Meteorol. Soc. Jpn.*, *93*, 5–48, doi:10.2151/jmsj.2015-001.

Kug, J. S., J. H. Jeong, Y. S. Jang, B. M. Kim, C. K. Folland, S. K. Min, and S. W. Son (2015), Two distinct influences of Arctic warming on cold winters over North America and East Asia, *Nat. Geosci.*, *8*, 759–762, doi:10.1038/ngeo2517.

Mori, M., M. Watanabe, H. Shigeo, J. Inoue, and M. Kimoto (2014), Robust Arctic sea-ice influence on the frequent Eurasian cold winters in past decades, *Nat. Geosci.*, *7*, 869–873, doi:10.1038/ngeo2277.

Nakamura, T., K. Yamazaki, K. Iwamoto, M. Honda, Y. Miyoshi, Y. Ogawa, and J. Ukita (2015), A negative phase shift of the winter AO/NAO due to the recent Arctic sea-ice reduction in late autumn, *J. Geophys. Res. Atmos.*, *120*, 3209–3227, doi:10.1002/2014JD022848.

Nakamura, T., K. Yamazaki, K. Iwamoto, M. Honda, Y. Miyoshi, Y. Ogawa, Y. Tomikawa, and J. Ukita (2016), The stratospheric pathway for Arctic impacts on midlatitude climate, *Geophys. Res. Lett.*, *43*, 3494–3501, doi:10.1002/2016GL068330.

Nishii, K., H. Nakamura, and T. Miyasaka (2009), Modulations in the planetary wave field induced by upward-propagating Rossby wave packets prior to stratospheric sudden warming events: A case study, *Q. J. R. Meteorol. Soc.*, *135*, 39–52, doi:10.1002/qj.359.

Ohfuchi, W., H. Nakamura, M. K. Yoshioka, T. Enomoto, K. Takaya, X. Peng, S. Yamane, T. Nishimura, Y. Kurihara, and K. Ninomiya (2004), 10-km mesh meso-scale resolving simulations of the global atmosphere on the Earth Simulator—Preliminary outcomes of AFES (AGCM for the Earth Simulator), *J. Earth Simul.*, *1*, 8–34.

Orsolini, Y. J., R. Senan, R. E. Benestad, and A. Melsom (2012), Autumn atmospheric response to the 2007 low Arctic sea ice extent in coupled ocean-atmosphere hindcasts, *Clim. Dyn.*, *38*, 2437–2448, doi:10.1007/s00382-011-1169-z.

Overland, J. E., and M. Wang (2010), Large-scale atmospheric circulation changes are associated with the recent loss of Arctic sea ice, *Tellus A*, *62*, 1–9, doi:10.1111/j.1600-0870.2009.00421.x.

Peings, Y., D. Saint-Martin, and H. Douville (2012), A numerical sensitivity study of the influence of Siberian snow on the northern annular mode, *J. Clim.*, *25*(2), 592–607, doi:10.1175/JCLI-D-11-00038.1.

Polvani, L. M., and D. W. Waugh (2004), Upward wave activity flux as a precursor to extreme stratospheric events and subsequent anomalous surface weather regimes, *J. Clim.*, *17*, 3548–3554, doi:10.1175/1520-0442(2004)017<3548:UWAFAA>2.0.CO;2.

Rayner, N. A., D. E. Parker, E. B. Horton, C. K. Folland, L. V. Alexander, D. P. Rowell, E. C. Kent, and A. Kaplan (2003), Global analysis of sea surface temperature, sea ice, and night marine air temperature since the late nineteenth century, *J. Geophys. Res.*, *108*(D14), 4407, doi:10.1029/2002JD002670.

Screen, J. A., I. Simmonds, C. Deser, and R. Tomas (2013), The atmospheric response to three decades of observed Arctic Sea ice loss, *J. Clim.*, *26*, 1230–1248, doi:10.1175/JCLI-D-12-00063.1.

Smith, K. L., and P. J. Kushner (2012), Linear interference and the initiation of extratropical stratosphere-troposphere interactions, *J. Geophys. Res.*, *117*, D13107, doi:10.1029/2012JD017587.

Sun, L., C. Deser, and R. A. Tomas (2015), Mechanisms of stratospheric and tropospheric circulation response to projected Arctic sea ice loss, *J. Clim.*, *28*, 7824–7845, doi:10.1175/JCLI-D-15-0169.1.

Takaya, K., and H. Nakamura (2001), A formulation of a phase-independent wave-activity flux for stationary and migratory quasigeostrophic eddies on a zonally varying basic flow, *J. Atmos. Sci.*, *58*, 608–627, doi:10.1175/1520-0469(2001)058<0608:AFOAPI>2.0.CO;2.

Thompson, D. W. J., and J. M. Wallace (1998), The Arctic Oscillation signature in the wintertime geopotential height and temperature fields, *Geophys. Res. Lett.*, *25*, 1297–1300, doi:10.1029/98GL00950.

Wu, Y., and K. L. Smith (2016), Response of Northern Hemisphere midlatitude circulation to Arctic amplification in a simple atmospheric general circulation model, *J. Clim.*, *29*, 2041–2058, doi:10.1175/JCLI-D-15-0602.1.

Yang, X. -Y., X. Yuan, and M. Ting (2016), Dynamical link between the Barents-Kara Sea ice and the Arctic Oscillation, *J. Clim.*, *29*, 5103–5122, doi:10.1175/JCLI-D-15-0669.1.